Ultrahigh strength magnesium *via* solidification of nanocolloid

Supplementary Information

Xinliang Yang[1], Hari Babu Nadendla[1*], Changming Fang[1], Shunsuke Nishi[2], Tomoki Matsuda[2], Makoto Kambara[2], Toshimi Tanaka[3], Masashi Dougakiuchi[2,4], Fengzai Tang[5], Geoffrey D. West[5], Shihao Wang[6,7*], Quentin M. Ramasse[6,7,8]

[1]BCAST, Brunel University of London, Kingston Lane, Uxbridge UB8 3PH, UK
[2]Division of Materials and Manufacturing Science, Graduate School of Engineering, The University of Osaka, 1-1 Yamadaoka, Suita, Osaka 565-0871, Japan
[3]Takeuchi Electric, 51-1, Hokuryo-cho, Matsue, 690-0816, Shimane, Japan
[4]Shimane Institute for Industrial Technology, 1 Hokuryo-cho, Matsue, 690-0816, Shimane, Japan
[5]WMG, University of Warwick, Coventry, CV4 7AL, UK
[6]SuperSTEM Laboratory, SciTech Daresbury Science and Innovation Campus, Keckwick Lane, Daresbury WA4 4AD, UK
[7]School of Chemical and Process Engineering, University of Leeds, Leeds LS2 9JT, UK
[8]School of Physics and Astronomy, University of Leeds, Leeds LS2 9JT, UK

*Corresponding authors: Hari Babu Nadendla, mtsthbn@brunel.ac.uk; Shihao Wang, swang@superstem.org

Contents

Supplementary Note

To achieve a stable nanocolloid in a molten magnesium medium (1000 K) with NbC nanoparticles of 15 nm diameter, the following conditions must be satisfied:

(i) The thermal energy associated with nanoparticle Brownian motion (E_b) must exceed the van der Waals attraction energy ($W_{vdWaals}$) between particles, ensuring dispersion rather than aggregation.

(ii) The energy barrier that prevents nanoparticle contact and sintering ($W_{barrier}$) must be greater than the Brownian motion energy (E_b), so that random collisions do not lead to irreversible bonding or clustering.

Thermal energy for nanoparticle dispersion. E_b is calculated to be 13.8 zJ ($E_b=kT$, where k is the Boltzmann constant and T is the processing temperature of 1000 K).

van der Waals attraction. The van der Waals interaction between two naked or coated NbC nanoparticles in molten Mg can be estimated by the equation[s1, s2]:

$$W_{vdWaals} = -\frac{A_{NbC-Mg(l)-NbC}}{6D} \cdot \frac{R_{NbC}}{2} \qquad \text{S1}$$

$$A_{NbC-Mg(l)-NbC} \approx \left(\sqrt{A_{NbC}} - \sqrt{A_{Mg(l)}}\right)^2 \qquad \text{S2}$$

where D, the minimum distance between two nanoparticles, is 0.2 nm (atomic layer of liquid Mg[s3]). R_{NbC}, the average radius of NbC nanoparticles, is 7.5 nm. $A_{Mg(l)}$ and A_{NbC} are the Hamaker constants of molten Mg and naked NbC for the van der Waals interaction. $A_{Mg(l)}$ is 206zJ for molten Mg[s4] and A_{NbC} is calculated to be 222 zJ using Lifshitz theory[s5, s6]. Therefore, the absolute value of the maximum van der Waals attraction ($W_{vdWaals}$) between two naked NbC nanoparticles in liquid Mg is estimated to be 0.94 zJ, which is less than the thermal energy for Brownian motion.

In the case of Mg-coated NbC particles (Mg@NbC), Prieve and Russel[s5] have demonstrated that coating can mask the substrate particle and alter the Hamaker constant of the substrate particles towards the value of the coating phase (here Mg phase) when the distance is very close ($D \to 0$). Thus, the value of $A_{NbC-Mg(l)-NbC}$ in equation S2 will be decreased significantly between particles in the molten Mg medium. Therefore, for Mg coated NbC particles in the molten Mg media, the Brownian motion dominates, and the particles will be unlikely to aggregate.

Energy barrier preventing naked nanoparticle contacting. At high temperatures, nanoparticles may sinter together upon contact, driven by a substantial reduction in interfacial energy. In a Mg(l)-Mg@NbC colloid, as shown in Fig. 3**a**, a stable C_{NbC}-like ordered Mg layer forms facilitated by ionic bonding between Mg and C on the outermost NbC {001} surface. For NbC_{nano} particles to make contact and sinter within the molten Mg, the Mg-C bonds at the Mg(l)/$NbC_{\{001\}}$ interface must be broken. The bonding energy of Mg-C is estimated using MgC in a rock salt-type structure[s7] due to its similar Mg-C bond lengths of 2.0-2.5 Å. The bonding energy[s8] is defined as $\Delta E = E_{(Mg-C)} - n \cdot E_{(Mg-Mg)}$, where $E_{(Mg-C)}$ and $E_{(Mg-Mg)}$ represent the bond energies of a single Mg-C bond in MgC and a single Mg-Mg bond in hcp Mg, respectively. The calculated average interfacial bonding energy for Mg-C is $-1.54\ \mathrm{J/m^2}$.

The debonding work ($W_{debonding}$) required for NbC_{nano} particles to come into contact and sinter is given by $W_{debonding} = S \cdot \sigma_{Mg-C}$, where S is the effective area of interaction (calculated as $S = \pi R D_0$ with R = 7.5 nm, and D_0 = 0.2 nm[s3]) and σ_{Mg-C} is the interfacial bonding energy. The resulting debonding work is calculated to be 7.25×10^3 zJ, which is approximately three orders of magnitude higher than the thermal energy (E_b=13.8 zJ). Consequently, the nanoparticles are unlikely to contact and sinter with one another under these conditions.

In brief, once naked NbC particles are introduced into liquid Mg, the formation of a Mg-coated layer on NbC leads to a stable Mg(l)-Mg@NbC nanocolloidal solution.

Assessment of colloid stability for larger particles:

The influence of gravity must be considered when assessing colloidal stability, particularly for larger particles. Stoke's equation[s9] is used to evaluate the sedimentation behaviour of the molten Mg-NbC system. Calculated sedimentation time shown in Supplementary Note Fig. 1**a** indicates that a 0.1 vol% suspension of micron-sized NbC particles requires approximately 10 hours to sediment through a 100 mm depth in the crucible. When the particle diameter decreases to 100 nm, the sedimentation time increases significantly to around 1000 hours, which exceeds the duration typical of standard foundry casting processes.

To justify the colloidal stability, an Mg-13 vol% $\mathrm{NbC_{micron}}$ colloidal solution was prepared by incorporating micron-sized NbC particles into molten Mg, followed by mechanical mixing using an impeller at 200 rpm. Then the suspension was held stationary for one hour before being allowed to solidify in the furnace under a slow, controlled cooling rate (see Supplementary Note Fig. 2). A local hardness measurement approach was used to assess the macroscopic uniformity of particle distribution. Supplementary Note Fig. 1**b** shows the spatial variation in Vickers hardness along the vertical cross-section of an ingot solidified from a Mg-13 vol% $\mathrm{NbC_{micron}}$ colloid. If sedimentation occurs, a sudden change in hardness would be observed. As seen in Supplementary Note Fig. 1**b**, the measured Vickers hardness remained consistent along the vertical section of the solidified ingot, indicating that no noticeable sedimentation occurred. This demonstrates that, despite the relatively large particle size, a stable Mg(l)-NbC colloid can be achieved.

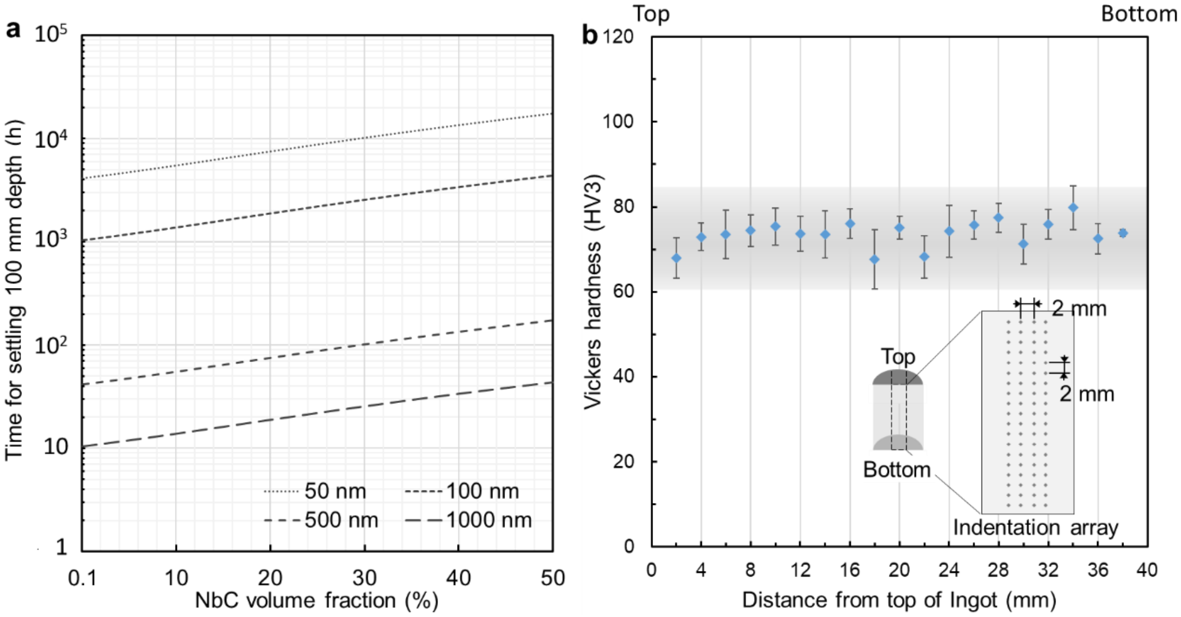

Supplementary Note Figure. 1 | The colloid stability assessment. **a,** The calculated settling time of NbC particles vs volume fraction. **b,** The Vickers hardness as a function of the position in the sample solidified from Mg-13vol%$\mathrm{NbC_{micron}}$ colloid. The unform hardness of the sample from top to the bottom of the as-solidified ingot suggesting stability of colloid without sedimentation of NbC particles at the bottom of the crucible.

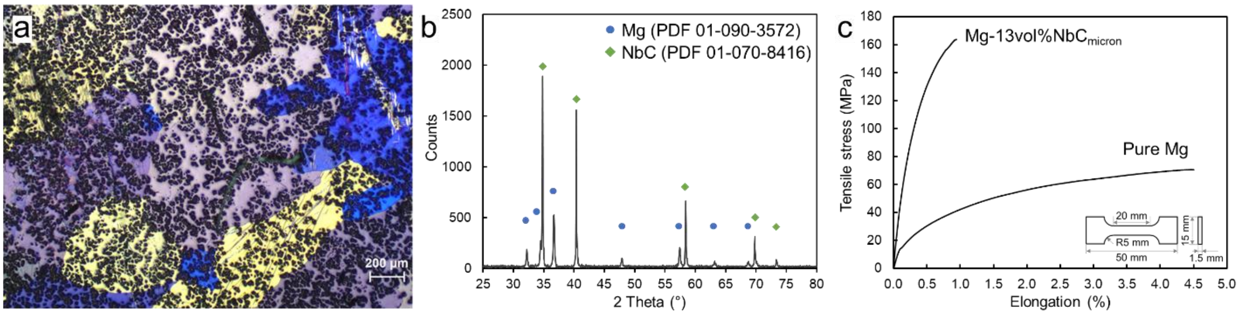

Supplementary Note Figure. 2 | The as-solidified sample from Mg-13vol%NbC$_{micron}$ colloid. **a,** Colour contrast represents the individual Mg grains with different orientation polarised optical microstructure. The dark spots in the Mg grains represent the NbC$_{micron}$ dispersions. **b,** XRD spectrum showing the phase constitution in this sample. **c**. Tensile stress-strain curves of the Mg-13vol%NbC$_{micron}$ sample and pure Mg sample under same solidification conditions.

Supplementary Table 1 | The properties of the published advanced metallic materials, which were used to plot Fig.2c.

	composition (wt%)	Tensile yield strength (MPa)	Ultimate tensile strength (MPa)	Elongation (%)	Elastic modulus (GPa)*	Density (g/cm³)
This work	$\text{Mg-NbC}_{\text{submicron}}$	584	678	10.1	130	4.14
	$\text{Mg-NbC}_{\text{nano}}$	436	526	11.9	82	2.53
Mg	Mg-3Al-1Zn-1Mn-0.5Ca[17]	219	306	17.0	45	1.77
	Mg-11Y-1Al[18]	350	394	8.0	47	1.93
	Mg-2Sn-2Ca[19]	443	460	1.2	45	1.80
	Mg-8Gd-3Y-0.4Zr[6]	650	710	4.5	45	1.96
	Mg-0.2Ca[20]	414	420	3.4	45	1.74
	Mg-6Zn-0.5 Zr[21]	310	351	17.1	45	1.83
Al	A7075-Zr[22]	373	417	3.8	66	2.81
	Al-5vol%MgO@GL[9]	486	549	9.1	85	2.74
	$\text{A2024-0.7wt\%Ti}_{\text{nano}}$[23]	286	432	10.0	73	2.78
	A7075[24]	734	774	2.8	71	2.81
Ti	Ti-8.5Cu[25]	1023	1180	2.1	120	4.65
	Ti-2.8Cr-4.5Zr-5.2Al[26]	1266	1413	12.6	109	4.58
	Ti-3.6Al-8V-6Cr-4Mo-4Zr[27]	1463	1611	5.4	106	4.80
	Ti-3.5Al-2.5V-2.5Sn-1.2Co-0.5Fe[28]	1177	1243	21.3	121	4.59
	Ti-6Al-4V[28]	759	1057	21.5	112	4.43
AHSS						
Maraging	Fe-18Mn-3Ti[1]	1626	1793	7.1	196	7.70
	Fe-19Ni-5Ti[29]	950	1300	10.0	190	7.89
	Fe-18Ni-3Al-4Mo[30]	1975	2113	9.0	186	7.99
	Fe-18Ni-3Al-4Mo-0.8Nb-0.08C-0.01B[31]	1973	2197	8.2	189	7.99
	Fe-9.9Cr-8.0Co-6.99Ni-1.8Al-2.75Mo-2.43W[32]	1892	2009	2.8	210	7.96
Martensitic	Fe-0.66C-1.42Cr-0.4Si-0.42Mn-0.07V[33]	2367	2613	7	208	7.87
	Fe-2.8Cr-1.07Ni-0.83Si-0.92Mo-0.76Mn-0.27C[34]	1110	1400	10.2	206	7.87
TRIP	Fe-0.1C-10Mn-1Si-0.3Mo-0.5V[35]	1012	1596	20.7	177	7.83
	Fe-0.47C-9.97Mn-0.7V-2.01Al[36]	1088	1761	16.6	196	7.83
	Fe-9.95Mn-0.44C-1.87Al-0.67V[37]	1978	2144	19.0	195	7.83
TWIP	Fe-22Mn-0.6C-4Cu[38]	701	1207	58.7	200	7.83
Nano-structured	Fe-24Mn-11Al-0.9C-5Ni[39]	1050	1300	39.3	176	6.48
	Fe-21Mn-10Al-1C-5Ni[40]	1273	1516	25.3	182	6.50
	Fe-5Ni-2Al-3Mn-1.5Cu-1.5Mo-1.5W-0.07Nb-0.05C-0.01B[41]	1365	1870	10.8	200	7.87
Complex phase	Fe-0.12C-0.28Si-2.3 Mn-0.01Ni-0.035Nb-0.64Cr-Ti-Mo[42]	859	1163	9.8	186	7.87

The presented properties of the advanced materials were extracted from the referred literatures. *The elastic modulus of the Mg-NbC samples were measured using the load-displacement curves during unloading period of the nanoindentations[s10].

Supplementary Table 2 | The microstructural information of the Mg-NbC materials.

	Mg average grain size (μm)*	NbC size (D_{50}) (nm)	NbC size spread (D_{10}-D_{90}) (nm)	NbC volume fraction (%)
Mg-NbC$_{nano}$	271	15	9-23	12.2
Mg-NbC$_{submicron}$	243	287	142-518	38.7
Mg-NbC$_{micron}$	530	906	500-1771	53.8

∗Mg grain size (equivalent circular diameter) was extracted from the EBSD data.

Supplementary Table 3 | Inputs for the Mg(l)/NbC interfaces for the AIMD simulations.

System	Shape of cell	Lattice parameters (Å)	Number of atoms	Surface polarity
Mg(l)/NbC$_{\{001\}}$	Tetragonal	a =13.52 c = 52.29	Mg: 300 Nb: 72 C: 72	Non-polar

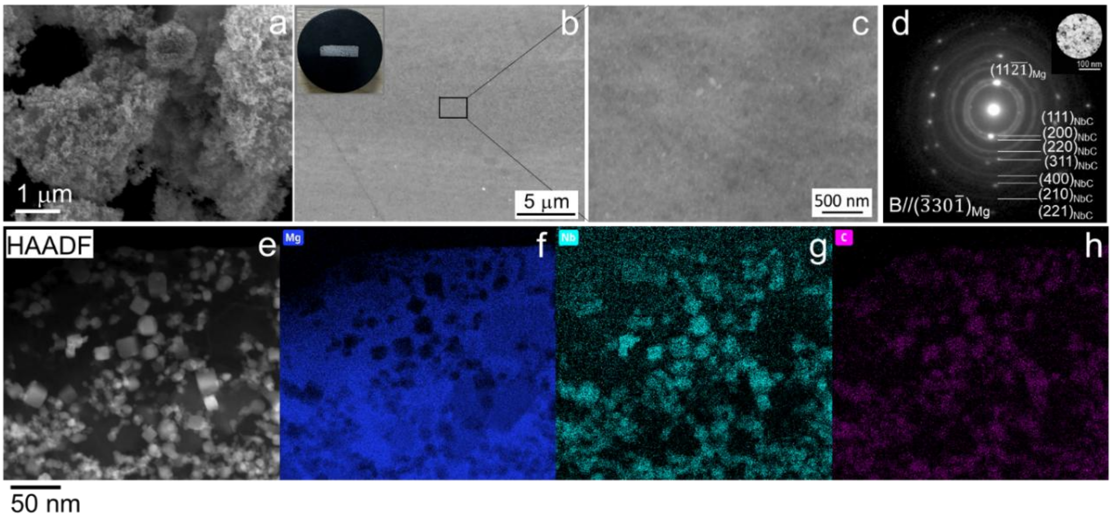

Supplementary Figure. 1 | The microstructure of Mg-NbC$_{nano}$ sample. **a,** SEM image of NbC$_{nano}$ particulates feedstock. **b,** SEM image of the as-solidified Mg-NbC$_{nano}$ sample showing uniform structure. The inset in **b** is cross-sectional image of pressure-less infiltrated and solidified bulk Mg-NbC$_{nano}$ sample mounted in Bakelite for metallography investigations. **c,** High magnification image of the region shown in **b** further confirming uniform structure. **d,** A selected area diffraction pattern from a Mg-NbC$_{nano}$ sample collected using TEM revealing the diffraction ring for NbC crystal together with the Mg pattern, suggesting presence of randomly oriented high number density of NbC nanoparticles within a Mg grain. The inset is the bright field TEM image shown the area (~200 nm diameter) that the diffraction pattern was taken. **e,** The HAADF-STEM image of the same sample, and corresponding STEM/EDS elemental maps of **f,** Mg; **g,** Nb; and **h,** C elements.

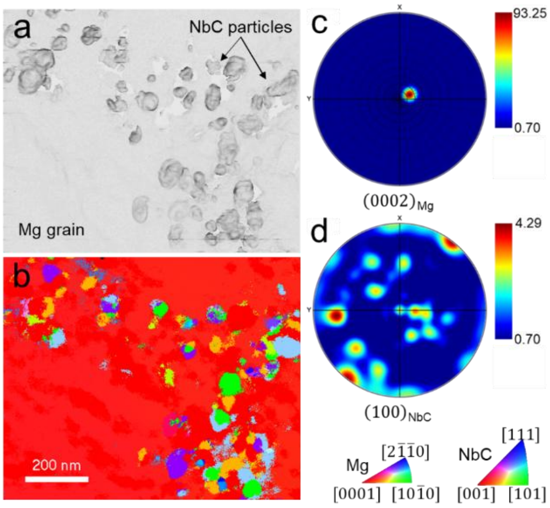

Supplementary Figure. 2 | The crystallographic analysis of Mg-NbC$_{nano}$ specimen *via* 4D-STEM showing the randomly orientated NbC in one Mg grain. **a,** Correlation coefficient map. **b,** inverse pole figure map. **c,** Mg pole figure in $(0002)_{Mg}$ pole. **d,** NbC pole figure in $(100)_{NbC}$ pole.

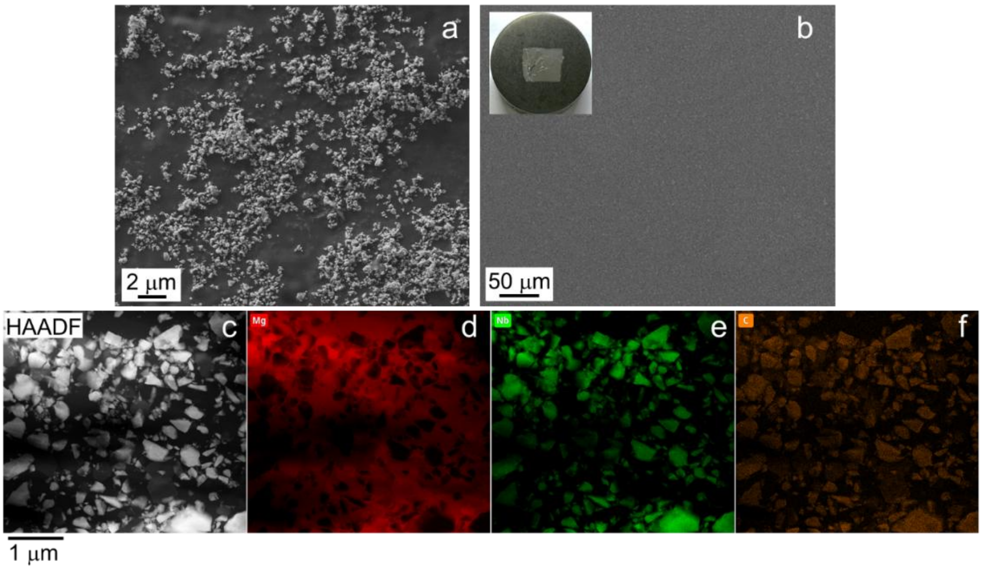

Supplementary Figure. 3 | The microstructure of Mg-NbC$_{\text{submicron}}$ sample. **a,** SEM image of NbC$_{\text{submicron}}$ feedstock, **b,** The SEM image of the as-solidified sample and the inset is the photograph of bulk sample. **c,** The HAADF-STEM image and corresponding STEM/EDS elemental maps of **d,** Mg; **e,** Nb; and **f,** C elements.

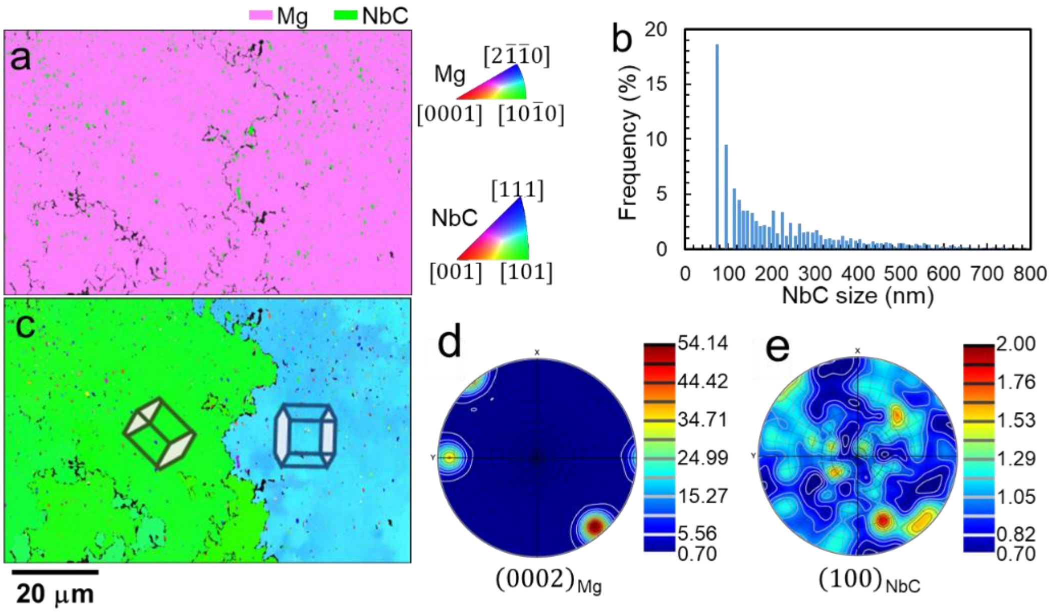

Supplementary Figure. 4 | Distribution of NbC$_{\text{submicron}}$ particle in the Mg matrix. **a,** Phase map of the Mg-NbC$_{\text{submicron}}$ specimen. **b**, The particle size distribution of the indexed NbC. The NbC particles with size lower than the indexing step size (80 nm) are not identified using EBSD method. **c**, The inverse pole figure map and its corresponding pole figures of the **d,** $(0002)_{\text{Mg}}$ pole, and **e,** $(100)_{\text{NbC}}$ pole. This investigation shows large number of the randomly oriented submicron NbC particles that are dispersed within Mg grains. The absence of particle segregation at grain boundaries indicates that the solidifying Mg front did not push sub-micron particles during solidification.

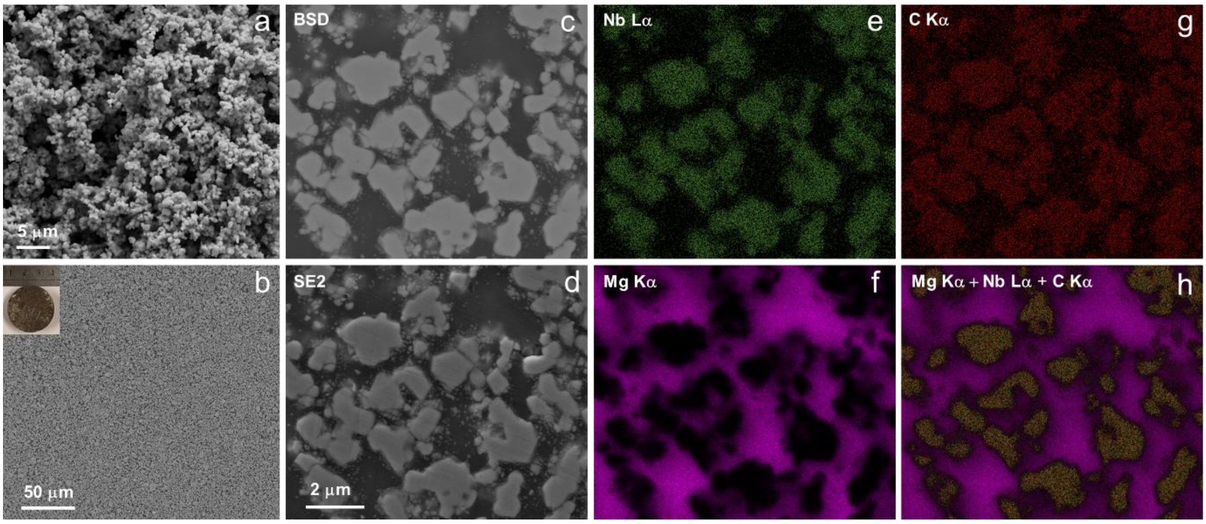

Supplementary Figure. 5 | The microstructure of Mg-NbC$_{\text{micron}}$ sample. **a,** SEM image of NbC$_{\text{micron}}$ particulates feedstock. **b,** SEM image of the as-solidified Mg-NbC$_{\text{micron}}$ sample showing uniform structure. The inset in **b** is the photo of pressure-less infiltrated and solidified bulk Mg-NbC$_{\text{micron}}$ sample with a 32 mm diameter. **c,** Higher magnification image of the sample shown in **b** showing micron scale NbC particle distribution in Mg matrix. **d-h,** Secondary electron image and the corresponding SEM/EDS elemental maps of **e,** Nb; **f,** Mg; **g,** C; and **h,** combined map for Mg + Nb + C elements.

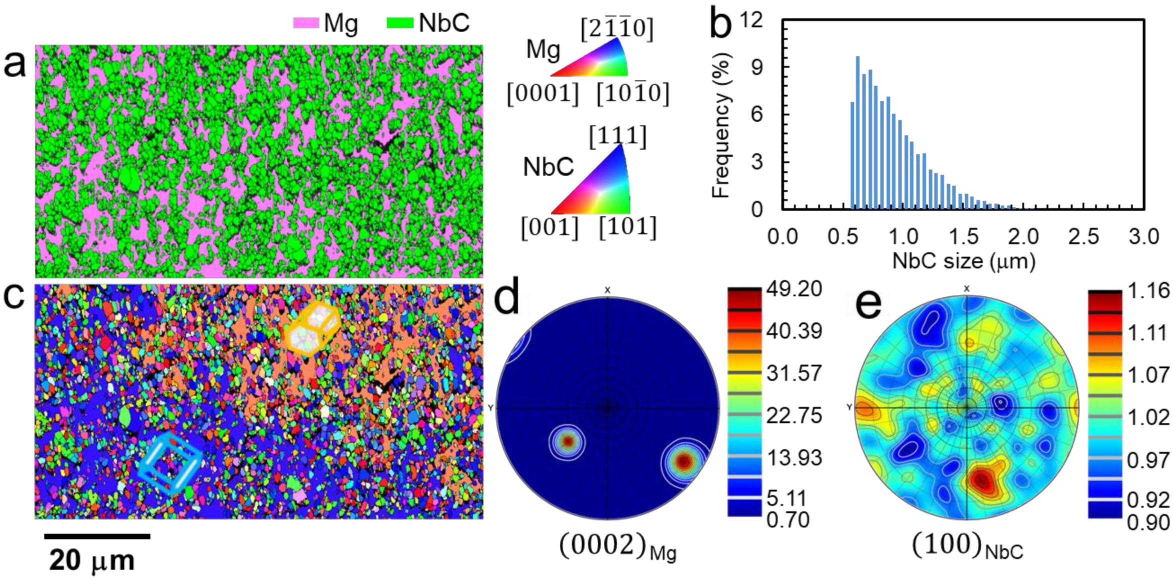

Supplementary Figure. 6 | Distribution of NbC$_{\text{micron}}$ particle in the Mg matrix. **a,** Phase map of the Mg-NbC$_{\text{micron}}$ specimen. **b**, The particle size distribution of the indexed NbC. **c**, The inverse pole figure map and its corresponding pole figures of the **d**, $(0002)_{Mg}$ pole; and **e**, $(100)_{NbC}$ pole. This investigation shows large number of the randomly oriented NbC$_{\text{micron}}$ particles dispersed within Mg grains.

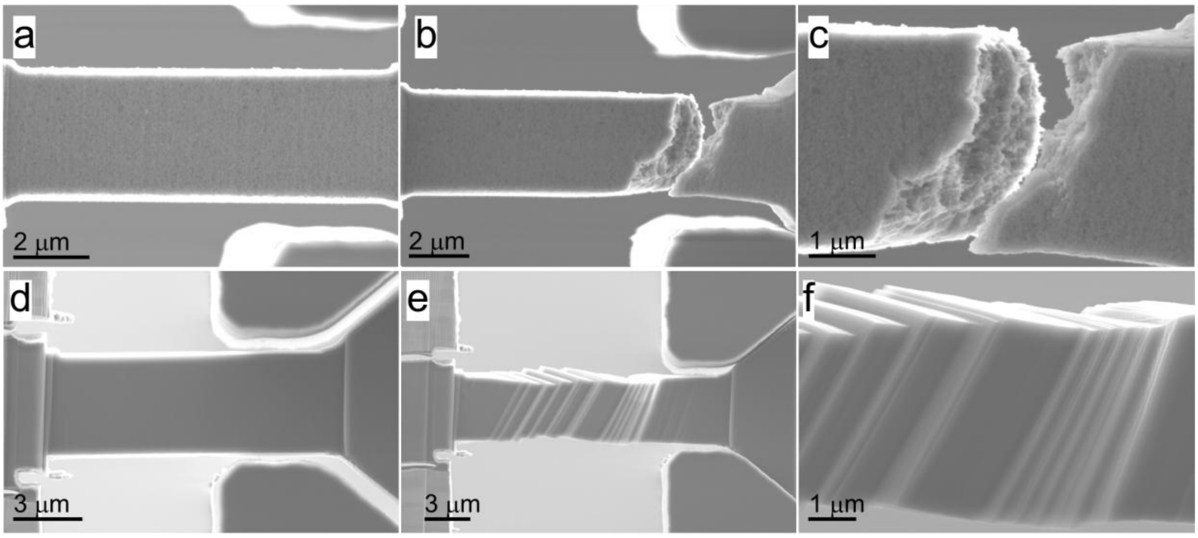

Supplementary Figure. 7 | SEM images of the micro-tensile samples. a, b, Mg-NbC$_{nano}$ specimen before and after tensile deformation. **c,** The enlarged image of fracture surface shown in **b**. **d, e,** Pure Mg specimen before and after tensile deformation. **f**, The enlarged image of basal slip activated area shown in **e**.

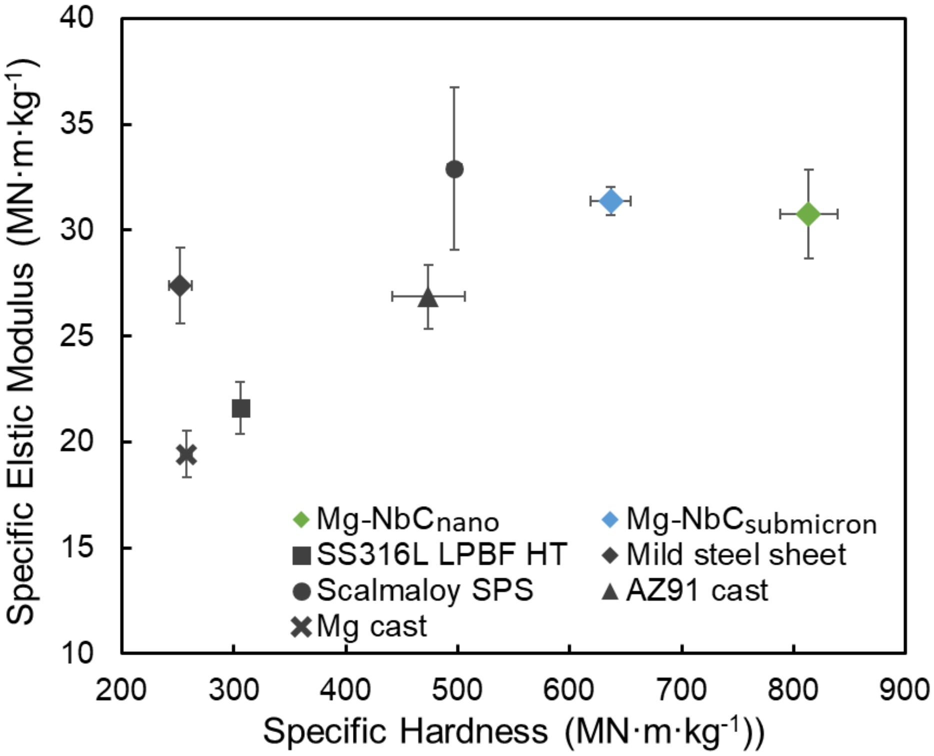

Supplementary Figure. 8 | Specific stiffness versus specific hardness of the Mg-NbC and engineering alloys. The nanoindentation test results of the Mg-NbC$_{nano}$ and Mg-NbC$_{submicron}$ show an advanced combination of the specific stiffness and hardness compared to the benchmark engineering alloys.

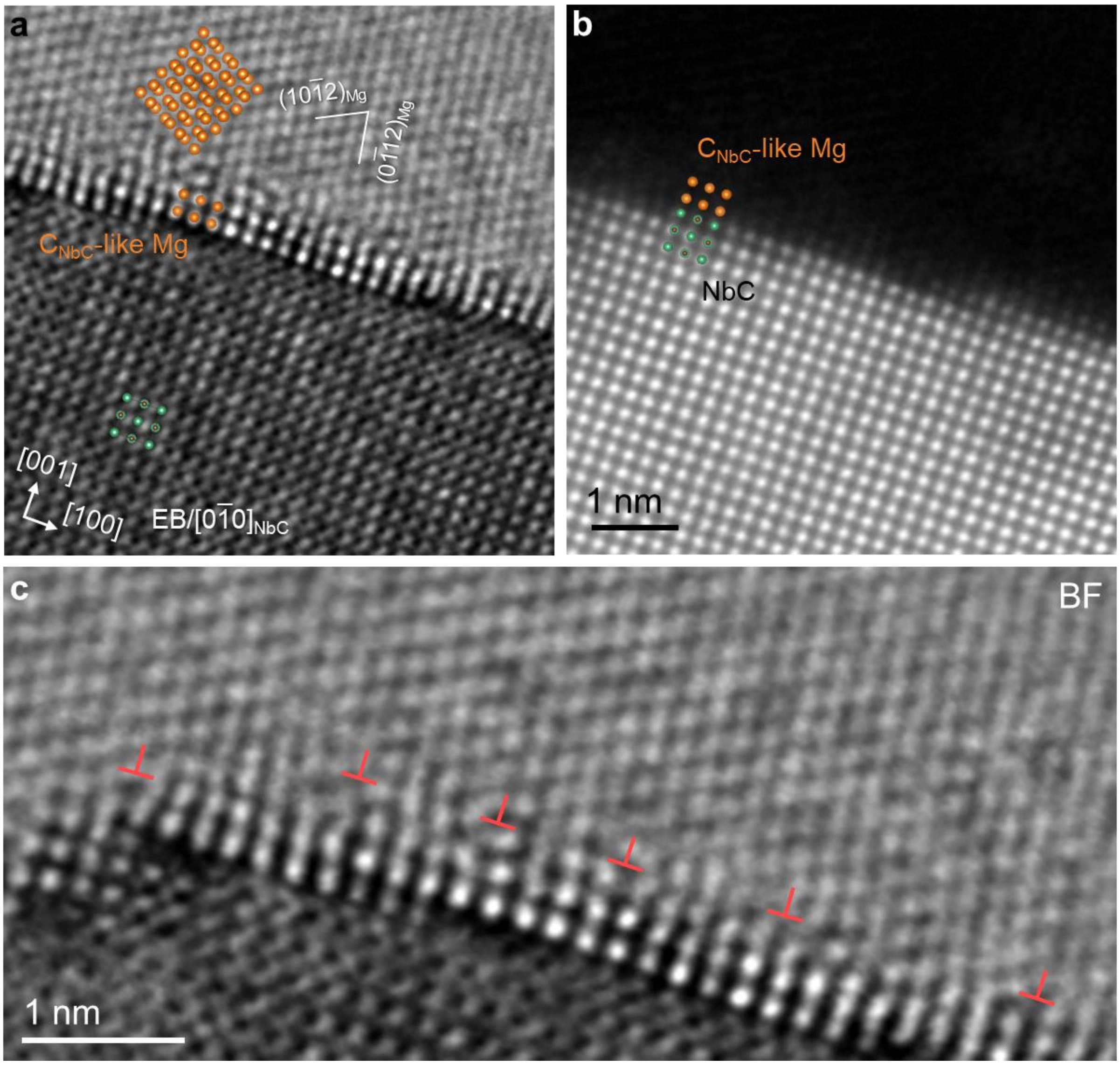

Supplementary Figure. 9 | The interfacial region of ordered C$_{\mathrm{NbC}}$-like Mg layer and follow-on HCP Mg crystal structure. **a.** The BF STEM image of interfacial area revealing the transitioning of atomic arrangements from the C$_{\mathrm{NbC}}$-like Mg terminating layer to the hexagonal close packed Mg crystal structure. **b,** the HAADF STEM image showing the interfacial area of NbC {001} surface and the C$_{\mathrm{NbC}}$-like Mg terminating ordered layer. **c**, the enlarged area in **a** exhibiting the microstructural transitioning across the interface, at which misfit dislocations are identified The incident beam is parallel to the zone axis [0-10]$_{\mathrm{NbC}}$, and close to the [-2201]$_{\mathrm{Mg}}$. Due to the presence of steps on NbC surface and the ordering behaviour of Mg, the scattered electron signals from the Mg terminal layer can overlap with that from NbC step when projected along either the <100> or <110> directions along the NbC {001} termination plane. This overlap results in the appearance of interfacial multilayer.

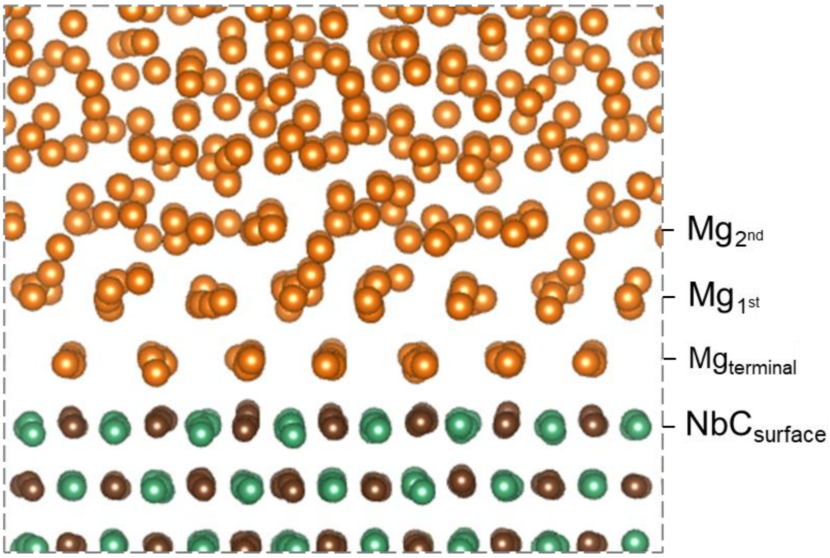

Supplementary Figure. 10 | Atomic arrangements of Mg(l)/NbC$_{\{001\}}$ interface. A snapshot of the atomic arrangements of Mg(l)/NbC{001} interface via <110>$_{NbC}$ direction equilibrated at 1000K. Green, brown and orange spheres represent Nb, C and Mg atoms, respectively.

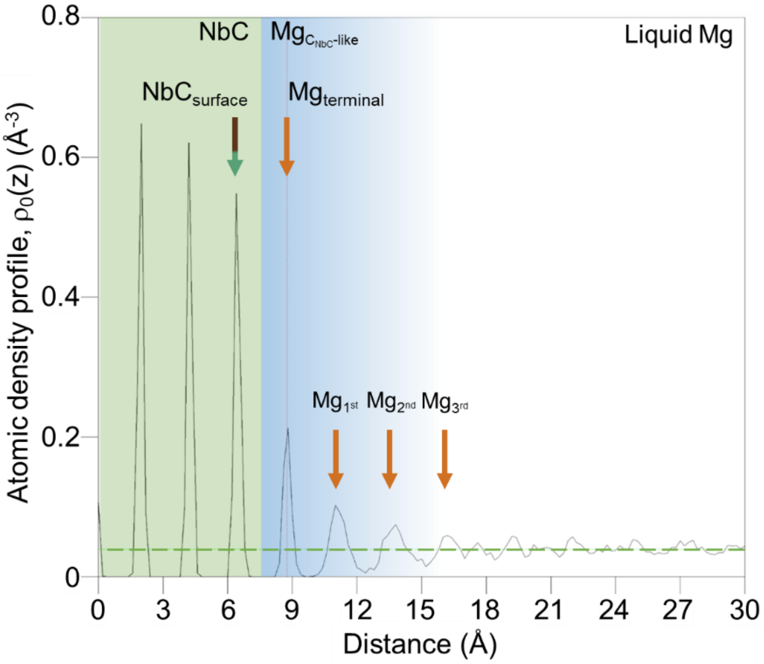

Supplementary Figure. 11 | The atomic density profile of Mg(l)/NbC$_{\{001\}}$ interface. There are three recognisable peaks. The terminating Mg atoms form one almost isolated symmetrical peak, marked by the red dotted line. The 1st peak is also symmetrical with reduced height. There is a finite atomic density between the 1st and the 2nd Mg layer. The 2nd peak is broad, consisting of a shoulder at 13.2 Å and a peak at 13.8 Å, indicating different stacking and bonding. There is a high density between the 2nd and 3rd Mg layer. The atomic density of 3rd Mg peak is close to the average value of liquid Mg (dashed green line). The atoms beyond 3rd peak behaves liquid like.

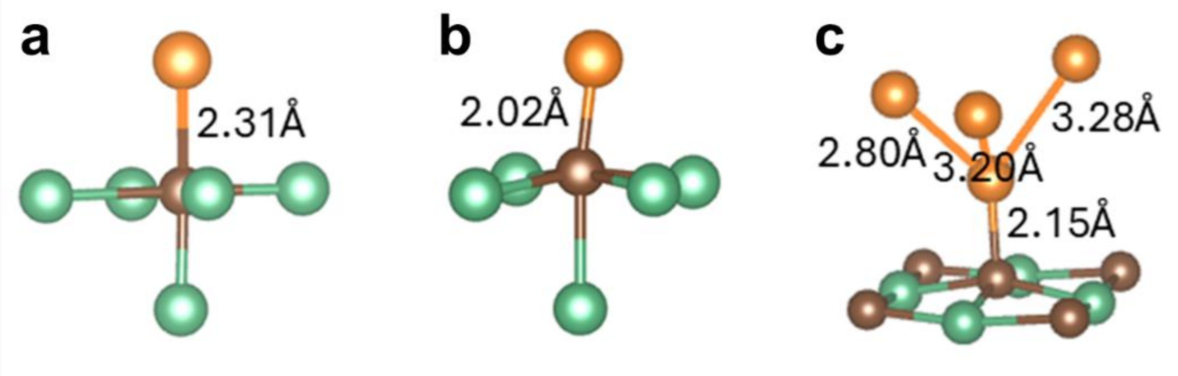

Supplementary Figure. 12 | Schematic atomic coordination of selected bond lengths for typical C atoms (the dark brown spheres). a, b, one Mg (the orange spheres) bonded to C atom at the Mg(l)/NbC$_{\{001\}}$ interfaces. The green spheres represent Nb atoms. **c**, schematic structure of atomic coordination of one terminating Mg atom in between outmost NbC$_{\{001\}}$ surface and 1st Mg layer.

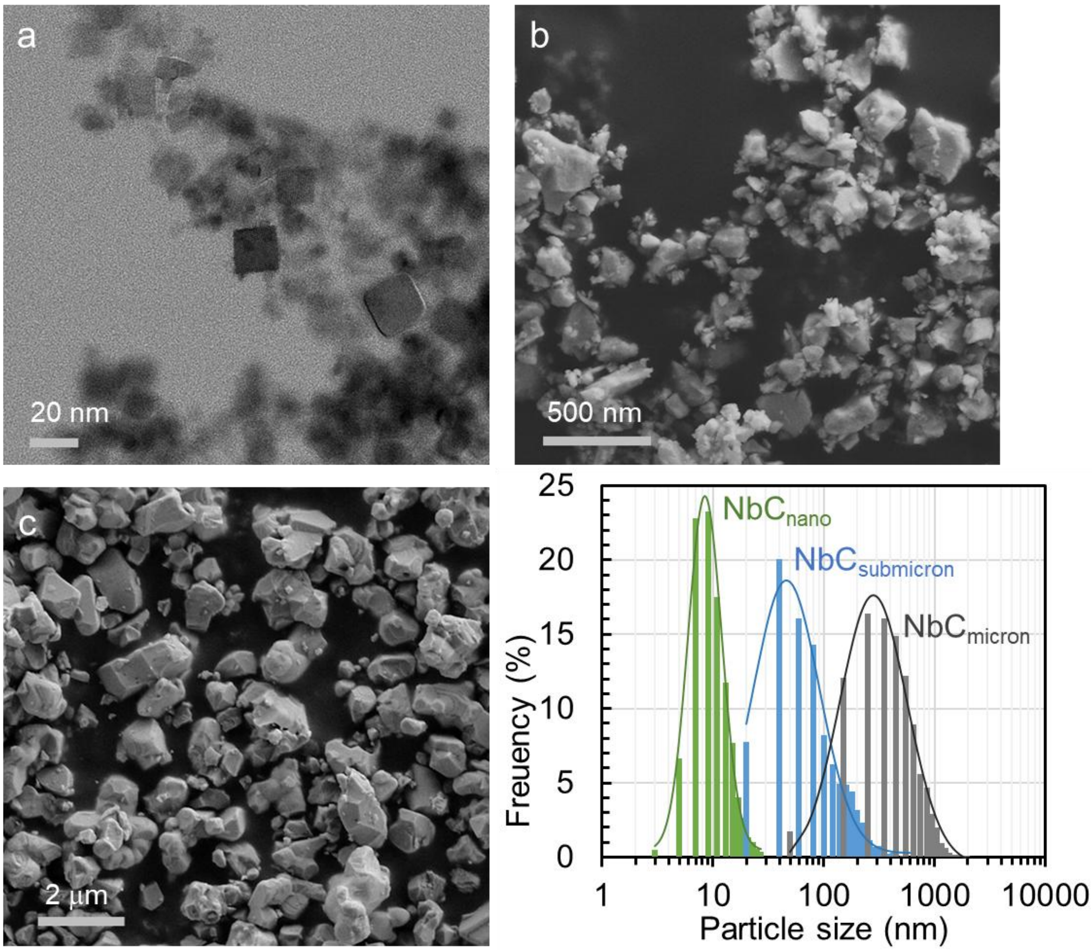

Supplementary Figure. 13 | NbC powder feedstock characterisation. **a,** TEM image of NbC$_{nano}$; **b,** SEM image of NbC$_{submicron}$; **c,** SEM image of NbC$_{micron}$, and **d,** their particle size distribution.

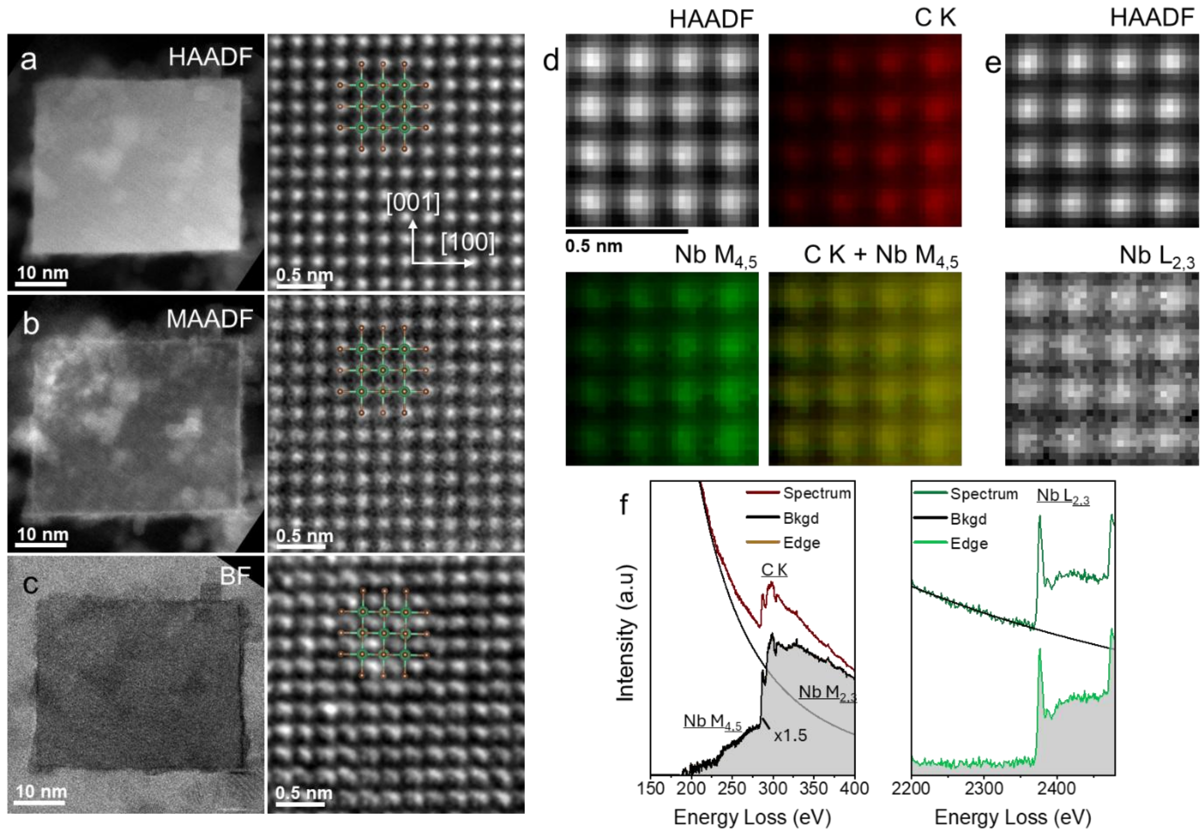

Supplementary Figure. 14 | $\mathrm{NbC_{nano}}$ observed *via* the $[0\text{-}10]_{\mathrm{NbC}}$ direction. a, HAADF STEM, **b,** MAADF STEM, **c,** BF TEM images at low and high magnification. **d,** HAADF image and corresponding EELS elemental maps of Nb $M_{4,5}$ edges, C *K* edge, and combined Nb + C map. **e,** HAADF image and corresponding STEM map of Nb element using Nb $L_{2,3}$ edges. **f,** EELS spectrums corresponding to **d** and **e**. The insets to (a-c) illustrate the atomic configuration of NbC crystal**,** where green, dark brown and orange spheres represent Nb, C and Mg atoms, respectively.

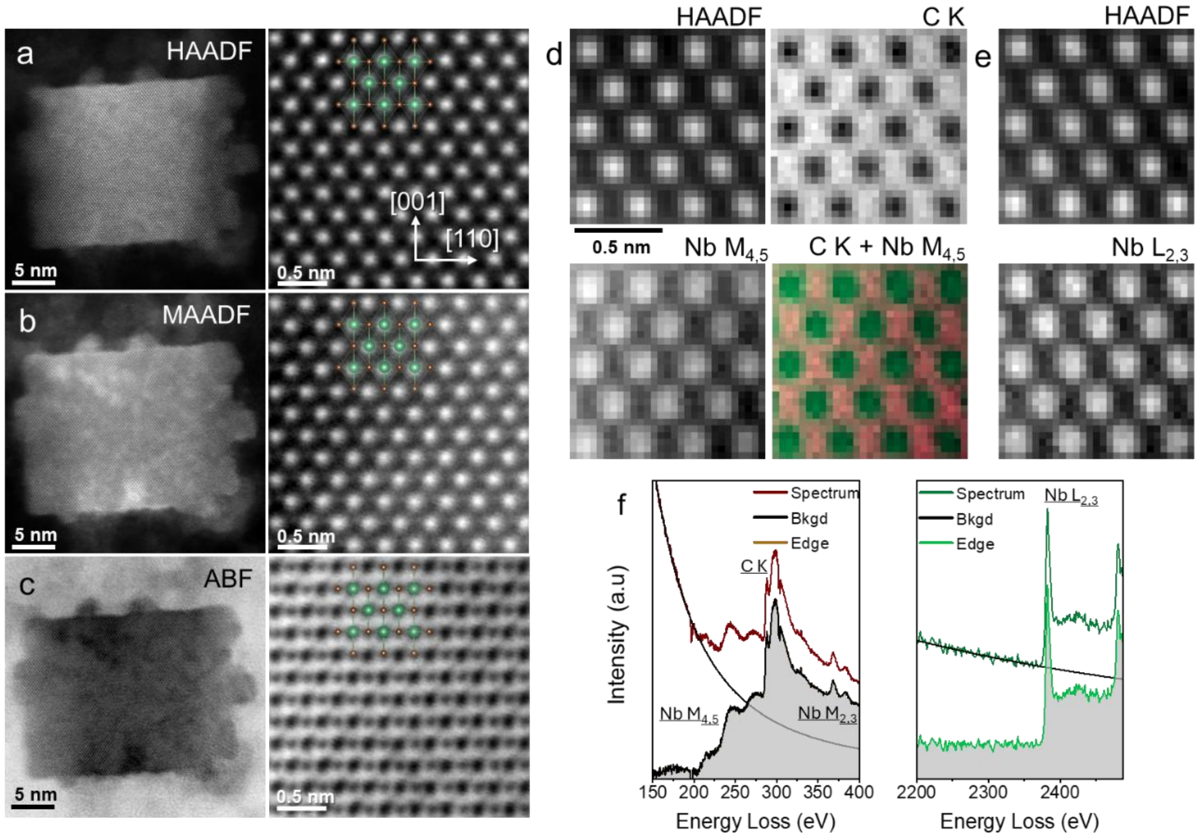

Supplementary Figure. 15 | NbC$_{nano}$ observed *via* the [1-10]$_{NbC}$ direction. a, HAADF STEM, **b,** MAADF STEM, and **c,** ABF STEM images at low and high magnification. **d,** HAADF image and corresponding EELS elemental maps of Nb $M_{4,5}$ edges, C K edge, and combined Nb + C map. **e,** HAADF image and corresponding STEM map of Nb element using Nb $L_{2,3}$ edges. **f,** EELS spectrums corresponding to **d** and **e**. The insets to (a-c) illustrate the atomic configuration of NbC crystal**,** where green, dark brown and orange spheres represent Nb, C and Mg atoms, respectively.

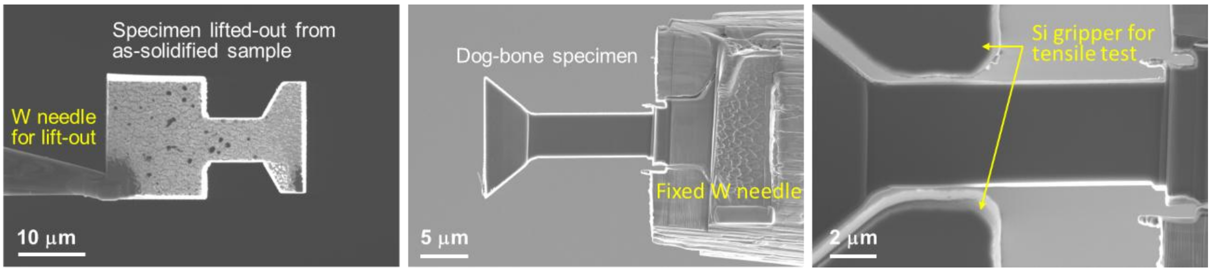

Supplementary Figure. 16 | The fabrication procedure of specimen for micro-tensile testing. **a,** Lift-out of the specimen from as-solidified sample. **b**, Attachment of the lift-out specimen to a preliminarily fabricated tungsten needle. **c**, Attachment of the silicon gripper for micro-tensile testing of the specimen.

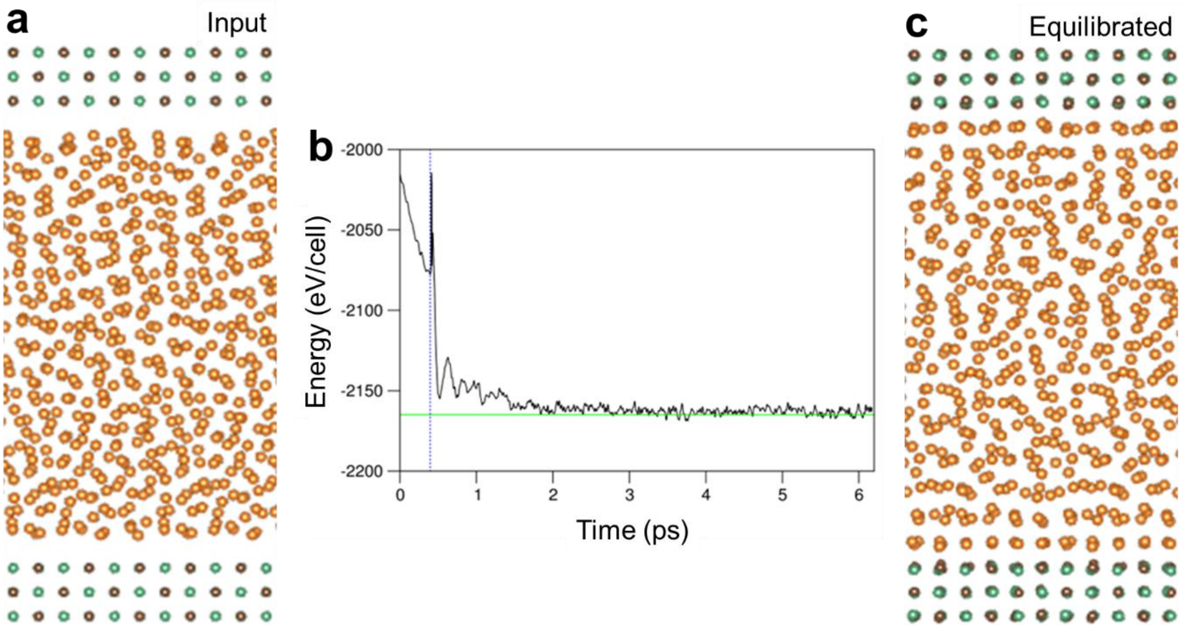

Supplementary Figure. 17 | Configuration of *ab initio* molecular dynamics (AIMD) simulation. a, Atomic arrangements for the input Mg(l)/$\text{NbC}_{\{001\}}$ interfaces. **b,** Dependence of the total valence electron energy on simulation time. **c,** Snapshots for the equilibrated Mg(l)/$\text{NbC}_{\{001\}}$ interface. Input configuration with setting of 2.0Å distance between the substrate atoms and the liquid Mg atoms leads the system in high energy state. A two-step approach was used: first AIMD simulations were performed with the substrate atoms fixed for about 300 steps (1.5 femtosecond (fs) per step). Then, the AIMD simulations are continued with relaxation of all the atoms. Once simulations start, the liquid Mg atoms were observed to be moving around. The liquid atoms near the NbC substrate were observed to move towards the fixed substrate atoms, gradually forming chemical bonding with the substrate atoms, forming an Mg coated NbC (Mg@NbC) surface. The energy decreases quickly with time. In the 2^{nd} step, when the substrate atoms are released, the energy rises sharply. Then it decreases quickly and then, gradually approaches the equilibrium value within another 2ps. Later, the total valence-electron energy of the system varies around the equilibrium value. When we equilibrated the system for another 4ps, the substrate atoms and the chemically bonded Mg atoms vibrate around their equilibrium positions, remaining solid-like. This indicates the high stability of Mg coated layer on the $\text{NbC}_{\{001\}}$ surface in liquid Mg.

Supplementary References

s1. Bergström, L. Hamaker constants of inorganic materials. *Adv. Colloid Interface Sci.* **70**, 125–169 (1997).

s2. Israelachvili, J. N. in *Intermolecular and surface forces* (Academic press, 2011).

s3. Sinnott, S. B. & Dickey, E. C. Ceramic/metal interface structures and their relationship to atomic- and meso-scale properties. *Materials Science and Engineering: R: Reports* **43**, 1–59 (2003).

s4. Xu, J. Q. et al. Theoretical study and pathways for nanoparticle capture during solidification of metal melt. *Journal of Physics: Condensed Matter* **24**, 255304 (2012).

s5. Prieve, D. C. & Russel, W. B. Simplified predictions of Hamaker constants from Lifshitz theory. *J. Colloid Interface Sci.* **125**, 1–13 (1988).

s6. Adachi, S. in *The Handbook on Optical Constants of Metals* 684 (WORLD SCIENTIFIC, 2012).

s7. Arblaster, J. W. in *Selected values of the crystallographic properties of elements* (ASM International, 2018).

s8. Brown, I. D. Recent Developments in the Methods and Applications of the Bond Valence Model. *Chem. Rev.* **109**, 6858–6919 (2009).

s9. Atiemo-Obeng, V. A. & Calabrese, R. V. Rotor–stator mixing devices. *Handbook of industrial mixing: Science and practice*, 479–505.

s10. Oliver, W. C. & Pharr, G. M. An improved technique for determining hardness and elastic modulus using load and displacement sensing indentation experiments. *J. Mater. Res.* **7**, 1564–1583 (1992).